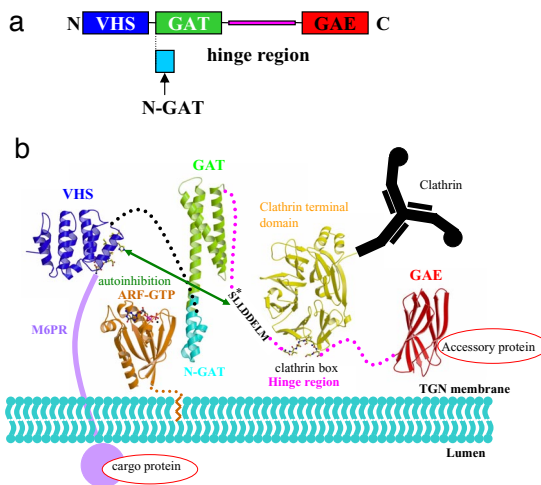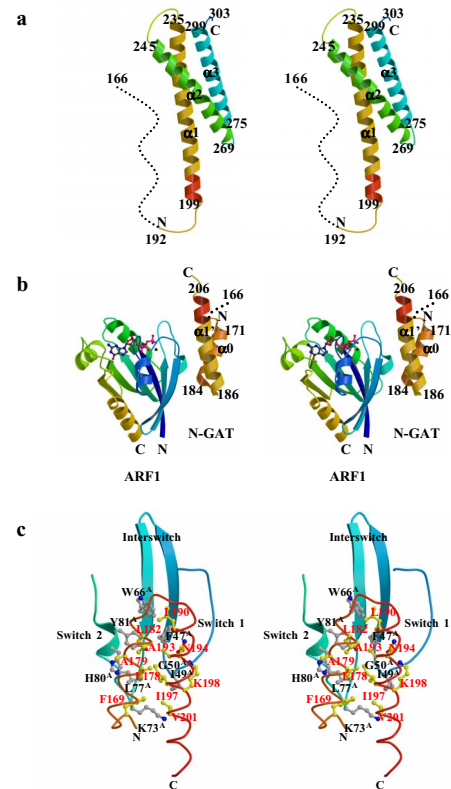# 8 Biological Science

8-1 Molecular Mechanism of the Membrane Recruitment of GGA by ARF in Lysosomal Protein Transport

The human body is made up of some 60 trillion cells containing membrane-bounded organelles such as nuclei, mitochondria, the endoplasmic reticulum (ER) and the Golgi apparatus, which perform specific functions using proteins, DNAs, RNAs and other biological molecules. Protein sequences are coded in DNA but many eukaryiotic proteins must be glycosylated (chemically linked to carbohydrates) after translation to become mature proteins and be transported to their final destinations. Poorly or wrongly glycosylated proteins cannot function because they cannot be transported to their work places or are regarded as unwanted and degrade swiftly. An intricate network of glycosylation, glycosidation (trimming carbohydrate residues), and protein transport systems achieves the complicated tasks of protein glycosylation in the ER and the Golgi, and of sorting via transport vesicles. A new class of adaptor proteins, GGAs (Golgi-localizing, γ-adaptin ear homology domain, ARF-binding proteins)

was found in 2000 and later demonstrated to facilitate the vesicular transport of lysosomal hydrolases which degrade unwanted glycolipids in lysosomes. All GGAs have a common domain organization: VHS, GAT and GAE domains (Fig. 1(a)). The lysosomal hydrolases first need to be modified with oligosaccharides with mannose 6-phosphate moiety for transport to lysosomes. Mannose 6-phosphate receptors (M6PR) collect lysosomal hydrolases correctly labeled with the mannose 6-phosphate groups in the trans-Golgi network. Next, adaptor proteins recognize the cargo-loaded M6PRs [1] and package them with clathrin. Clathrin coated transport vesicles are then transported to early lysosomes which become mature lysosomes. The GGA-GAE domains modulate the packaging and membrane fusion processes through interactions with accessory proteins [2].

Figure 1
Domain organization of GGA and the proposed model of the interactions with its partners during vesicle formation. (a) Schematic representation of the domain organization of human GGA proteins and N-GAT. (b) Model of GGA proteins with its domains interacting with M6PR, ARF-GTP, clathrin N-terminal propeller and an accessory protein. The VHS domain recognizes sorting signals such as M6PR (PDB: 1JWG). The GAT domain interacts with a membrane-bound ARF (in this study). The subsequent hinge region interacts with clathrin (clathrin terminal domain complexed with clathrin-box peptide from β3-hinge of AP-3, PDB: 1C9I). The sequence S*LLDDELM interacts with the VHS domain (autoinhibition) when S* is phosphorylated. Finally, the C-terminal GGA1 GAE domain is modeled from the structure of the ear domain of γ-adaptin ([2], PDB: 1IU1) based on their similarity both in sequence and function.

Figure 2
Structures of the GGA1-GAT domain and its complex with ARF1. (a) Stereo diagram of the GGA1-GAT domain. The GAT domain forms three α-helices connected by loops of varying length. The final model is complete except for the N-terminal 26 residues (166-191: dotted line) and the C-terminal 2 residues (304-305) whose electron density is very weak. (b) Stereo diagram of the ARF1/N-GAT complex. N-GAT forms a helix-loop-helix motif facing the Switches 1 and 2 of ARF1-GTP. Diagrams a and b are shown in the same orientation, chosen by a least-squares minimization of the overlap of a common helical region (199-205, shown in red in a and b) between the GAT domain and the ARF1/N-GAT complex. (c) Stereo diagram of the ARF1/N-GAT interface. Ball-and-stick models in yellow with red labels represent residues of N-GAT which interact with ARF1, and A193 which is located in hydrophobic core formed by α0 and α1'. Ball-and-stick models in gray with black labels show residues of ARF1 which interact with N-GAT.

ARF-GTP bound to trans-Golgi network membranes recruits its effector, the GAT domain of GGA, thus making it easier for GGA to recognize the cargo-loaded receptors. Here we report the X-ray crystal structures of the human GGA1-GAT domain and the complex between ARF1 (ADP-ribosylation factor) and the N-terminal part of the GAT domain [3]. When unbound, the GAT domain forms an elongated bundle of three α-helices with a hydrophobic core (Fig. 2(a)). When combined with the preceding VHS domain, this domain structurally resembles CALM, an AP180 homolog involved in endocytosis, implying a canonical structural motif prevalent in vesicle transport. In the complex with ARF1-GTP, a helix-loop-helix of the N-terminal part of GAT (N-GAT) interacts with the switches 1 and 2 of ARF1 predominantly in a hydrophobic manner (Fig. 2(c)).

Incidentally, three other groups from the US National Institute of Health (NIH) [4], Cambridge University [5] and Oklahoma University [6], reported the structures of the GGA1-GAT domain separately within a period of 2 months. The structure reported by the NIH group is very similar to ours, but the other two studies report that the GAT domain folds into a 4-helix structure which resembles our combined model of the N-terminal GAT domain in complex with ARF1-GTP and the GAT domain alone. Along with our circular dichroims data which shows a partially folded state of the N-terminal part of the GAT domain, we believe that this part is in equilibrium between an α helix and a disordered random coil, and that the interaction with ARF fixes it in the 4-helix structure for secure docking onto the TGN membrane. Our N-GAT/ARF structure differs from any of the ARF complexes reported so far, and indeed serves as the first reported structure of the complex between ARF and its effector. These data reveal a molecular mechanism underlying the membrane recruitment of adaptor proteins by ARF-GTP, which then facilitates the recruitment of cargo-bound receptors (Fig. 1) followed by clathrin-coated transport vesicle formation, budding, and membrane fusion.

T. Shiba[1], M. Kawasaki[1], H. Takatsu[2,3], T. Nogi[1,4], N. Matsugaki[1], N. Igarashi[1], M. Suzuki[1], R. Kato[1], K. Nakayama[2,5] and S. Wakatsuki[1] ([1]KEK-PF, [2]Univ. of Tsukuba, [3]RIKEN, [4]Max Planck Inst., [5]Kyoto Univ.)

References
[1] T. Shiba, H. Takatsu, T. Nogi, N. Matsugaki, M. Kawasaki, N. Igarashi, M. Suzuki, R. Kato, T. Earnest, K. Nakayama and S. Wakatsuki, *Nature* **415** (2002) 937.
[2] H. Takatsu, K. Yoshino and K. Nakayama, *Biochem. Biophys. Res. Commun.* **271** (2000) 719.
[3] T. Shiba, M. Kawasaki, H. Takatsu, T. Nogi, N. Matsugaki, N. Igarashi, M. Suzuki, R. Kato, K. Nakayama and S. Wakatsuki, *Nat. Struct. Biol.* **10** (2003) 386.
[4] S. Suer, S. Misra, L.F. Saidi and J.H. Hurley, *Proc. Natl. Acad. Sci.* **100** (2003) 4415.
[5] B.M. Collins, P.J. Watson and D.J. Owen, *Dev. Cell* **4** (2003) 321.
[6] G. Zhu, P. Zhai, X. He, S. Terzyan, R. Zhang, A. Joachimiak, J. Tang and X.C. Zhang, *Biochemistry* **42** (2003) 6392.

8-2 Structure of the Protein-Degradation Mediating Mammalian 20S Proteasome

The proteasome is the central mediator of nonlysosomal protein degradation in both the cytosol and the nucleus and is involved in the degradation of both misfolded proteins and short-lived regulatory proteins. The 26S proteasome consists of a central cylindrical 20S proteasome containing 28 subunits as a catalytic machine with a molecular mass of 700 kDa, and two large regulatory complexes termed PA700 (Proteasome Activator 700). The 26S proteasome, with a molecular mass of approximately 2 MDa, degrades target proteins flagged with poly-ubiquitin (the ubiquitin-proteasome system). This degradation requires ATP hydrolysis. The crystal structures of the 20S proteasome, from the archaea *Thermoplasma acidophilum* [1] and yeast *Saccharomyces cerevisiae* [2] were solved in 1995 and 1997. The proteasome structure in higher eukaryotic organisms, however, has not yet been determined. In higher eukaryotes, the proteasome acts as an antigen-processing enzyme, responsible for the generation of peptides presented by MHC class I molecules. Moreover, the mammalian 20S proteasome has three active subunits, $\beta1$, $\beta2$, and $\beta5$, which are replaced in the immunoproteasome by interferon-γ-inducible subunits $\beta1i$, $\beta2i$, and $\beta5i$.

To elucidate the sophisticated molecular mechanism underlying the mammalian proteasome and to study how it differs from the proteasome in lower organisms, we have analyzed the crystal structure of the 20S proteasome from bovine liver [3]. Data collection was performed at several synchrotron radiation facilities. Since the isomorphism between crystals was very poor, the partial datasets could not be combined. Only one crystal out of more than 1,000 was suitable for successful structure determination. The crystal belonged to the space group $P2_12_12_1$ with cell dimensions of $a = 315.7$ Å, $b = 205.9$ Å, and $c = 116.0$ Å. The R_{merge} was 9.5% with 96.3% completeness between 100 and 2.75 Å resolution. One 20S proteasome molecule was in an asymmetric unit. The structure was determined with the molecular replacement method using the structure of the yeast proteasome as a model. The overall shape of the bovine 20S proteasome was an elongated cylinder having large central cavities and narrow constrictions (Fig. 3). Its overall dimensions were approximately 150 Å in length and 115 Å in diameter, a size that has been conserved from the *T. acidophilum* and yeast proteasome. The electron density map of the bovine proteasome clearly distinguished the constitutive subunits from the γ-interferon inducible ones. Furthermore, the bovine 20S proteasome was confirmed to have an identical arrangement of subunits as the yeast proteasome.

The structures of the $\beta2$, $\beta1$, $\beta5$, $\beta6$, and $\beta7$ subunits of the bovine enzyme were different from the yeast

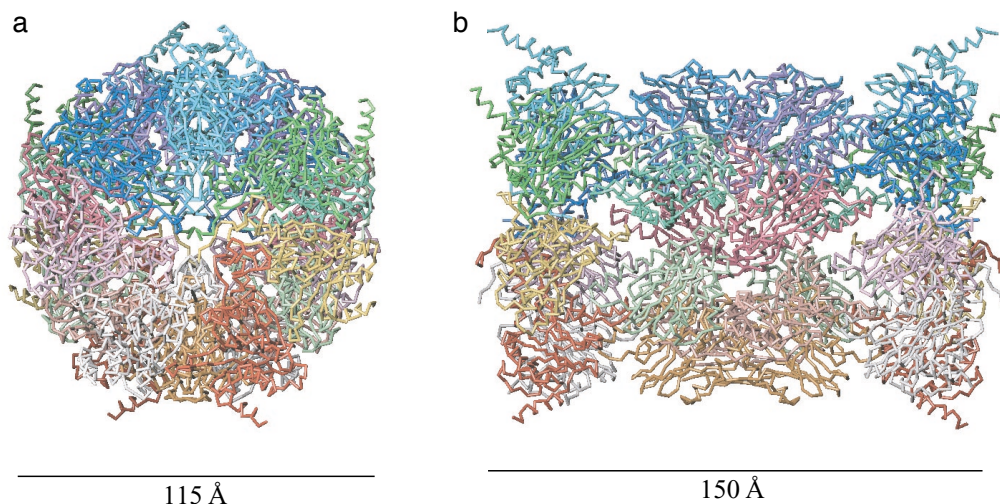Figure 3

Cα drawings of the bovine 20S proteasom. The enzyme consists of 28 subunits, $[(\alpha1-\alpha7)(\beta1-\beta7)]_2$. Fourteen of the different subunits are shown in different colors; α1, red; α2, yellow; α3, green; α4, sky blue; α5, blue; α6, pink; α7, gray; β1, orange; β2, dark sea green; β3, medium sea green; β4, dark sky blue; β5, purple; β6, magenta; and β7, light pink. (a) Top view, (b) Side view.

enzyme, enabling the bovine proteasome to accommodate either constitutive or inducible subunits. A novel N-terminal nucleophile hydrolase activity was proposed for the β7 subunit. We also determined the location of the nuclear localization signals (NLS) within the molecule. A model of the immunoproteasome can be predicted from this constitutive structure. Based on the predicted model of the immunoproteasome, we can understand the mechanism by which the immunoproteasome enhances the activity for antigen presentation more than the constitutive 20S proteasome.

M. Unno and T. Tsukihara (Osaka Univ.)

References

[1] J. Lowe, D. Stock, B. Jap, P. Zwickl, W. Baumeister and R. Huber, *Science* **268** (1995) 533.
[2] M. Groll, L. Ditzel, J. Lowe, D. Stock, M. Bochtler, H.D. Bartunik and R. Huber, *Nature* **386** (1997) 463.
[3] M. Unno, T. Mizushima, Y. Morimoto, Y. Tomisugi, K. Tanaka, N. Yasuoka and T. Tsukihara, *Structure* **10** (2002) 609.

8-3 A Novel Interacting Mechanism between Mammalian Protein Phosphatase 1 and its Inhibitor Calyculin A

Protein phosphatase 1 and 2A (PP1 and PP2A) are two of the four major enzymes that dephosphorylate serine and threonine residues of proteins in the cytosol of eukaryotic cells [1]. The catalytic subunits of PP1 (PP1c) and PP2A are subjected to inhibition by various toxins, the so-called okadaic acid class of compounds, including okadaic acid, microcystin-LR (MCLR), and calyculin A. Among these inhibitors, calyculin A has a unique structure, consisting of a polyketide and a dipeptide with a phosphate group in the polyketide portion, and is known to adopt a pseudocyclic conformation by forming intramolecular bonds in the solid state as well as in solution. X-ray

crystallography of the catalytic subunit of PP1 (α-isozyme; PP1α) complexed with MCLR, which was the first structure solved of the complex of PP1c and inhibitor, provided a detailed view of the interaction between the enzyme and the toxin [2]. In addition, a recent crystallographic study shows that okadaic acid is also accommodated into PP1γ (γ-isozyme of PP1) with essentially the same binding mode as MCLR [3]. Several binding models for calyculin A, as well as those for the other inhibitors, have been proposed on the basis of this crystal structure. Many of these models postulated that calyculin A is accommodated into the binding pocket for MCLR in such a way that the head component of calyculin A including the phosphate group forms hydrogen bonds or indirect coordinate bonds with the amino acid residues around the catalytic center, whereas the nonpolar polyketide tail is docked in the hydrophobic surface groove that extends from the catalytic center. However, calyculin A has a very flexible backbone structure, and these models are purely speculative.

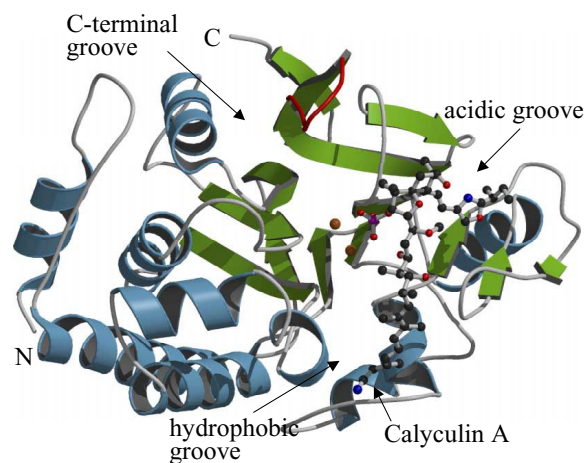The crystal structure of the complex between the PP1 catalytic subunit (PP1γ) and calyculin A has been

Figure 4
Overall structure of PP1γ-calyculin A complex.

Arg96

Calyculin A
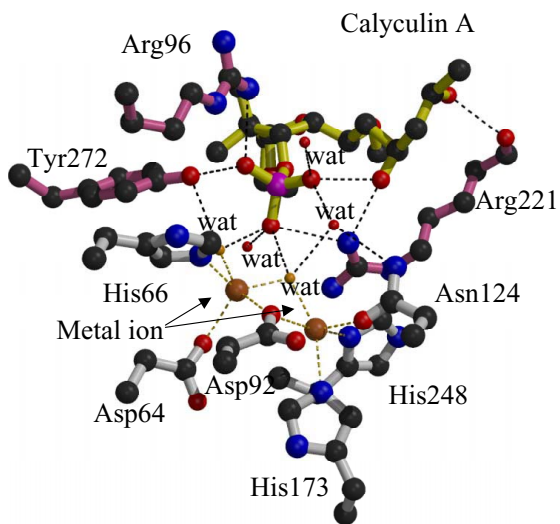
Tyr272

wat wat

wat wat

wat

His66

Arg221

Metal ion

Asn124

Asp92

His248

Asp64

His173

determined at 2.0 Å resolution, showing direct evidence for understanding the general mechanism of the PP1 inhibition [4]. On the molecular surface, there are three grooves (the hydrophobic groove, acidic groove, and C-terminal groove) connected at the bifurcation point (Fig. 4). PP1γ has two metal ions, located at the bifurcation point, and this point is assumed as the catalytic center. Calyculin A is located in the hydrophobic groove and the acidic groove in an extended form. This is the first observation to note that the inhibitor adopts not a pseudocyclic conformation but an extended conformation in order to form a complex with the protein. The phosphate group of calyculin A is also located at the bifurcation point, and the metals, ligand atoms, water molecules, and phosphate group form a close network (Fig. 5). It should be mentioned that Arg96, Arg221 and Tyr272 of PP1γ make direct interactions with calyculin A and that they play important roles in holding the phosphate group. The region between the C33 and C37 atoms of calyculin A, which is supposed to have large flexibility in the crystal form, could not be located due to unclear electron density. It is found that the inhibitory effect on the phosphatase activity of PP1γ between calyculin A and hemicalyculin A, which lacks the C29-C37 component of calyculin A, is quite similar. These structural features are consistent with the findings from dose-inhibition analysis studies.

A. Kita [1] and K. Miki [1,2] ([1] Kyoto Univ., [2] RIKEN)

References
[1] P. Cohen, *Annu. Rev. Biochem.* **58** (1989) 453.
[2] J. Goldberg, H.B. Huang, Y.G. Kwon, P. Greengard, A.C. Nairn and J. Kuriyan, *Nature* **376** (1995) 745.
[3] J.T. Maynes, K.S. Bateman, M.M. Cherney, A.K. Das, H.A. Luu, C.F. Holmes and M.N. James, *J. Biol. Chem.* **276** (2001) 44078.
[4] A. Kita, S. Matsunaga, A. Takai, H. Kataiwa, T. Wakimoto, N. Fusetani, M. Isobe and K. Miki, *Structure* **10** (2002) 715.

8-4 The Molecular Mechanism of Plasmodium Wound Healing, Triggered by Ca²⁺ Binding Protein 40, CBP40

The lower eukaryote *Physarum polycephalum* changes morphology during its life cycle which includes the amoeba and plasmodia phases. Plasmodium is a giant creeping single cell, and is characterized by vigorous cytoplasmic streaming. Therefore, the wound healing process is indispensable for the survival of plasmodia. Plasmodia have a unique sealing system; when the cytoplasm is exposed to extracellular fluid, the calcium binding protein 40 (CBP40) seals damaged areas forming large aggregates Ca^{2+}-dependently [1]. CBP40 contains four EF-hand motifs and 218 residues in the N-terminal region. Part of the CBP40 is truncated N-terminal 32 residues by a proteinase in plasmodia (CBP40Δ), which does not aggregate in the Ca^{2+}-bound form. In order to elucidate the mechanism of the Ca^{2+}-dependent oligomerization of CBP40, we have determined the crystal structures of CBP40Δ in both the metal-free and the Ca^{2+}-bound states at 3.0 Å resolution [2,3].

Both structures consist of three domains: coiled-coil, intervening and EF-hand (Fig. 6). The N-terminal coiled-coil domain is comprised of helices 1 and 2. In the Ca^{2+}-bound form, the omit map confirmed that four Ca^{2+} are bound at the four EF-hands. On the other hand, the omit map of the metal-free form showed that there is negligible Ca^{2+} remaining. The topology of the EF-hand domain is similar to that of the penta-EF-hand (PEF) protein family such as calpain. But, CBP40 does not have a fifth EF-hand. The structure of the metal-free form is almost identical with that of the Ca^{2+}-bound form, except for minor perturbations of the EF-hand loops. Since CBP40 has no linker loop between EF1/EF2 and EF3/EF4, these hands interact closely to form a stable and highly compact structure. This may be the reason why a large conformational change as calmodulin does not occur in CBP40. The large hydrophobic interface of the EF-hand domain with the N-terminal half is important for the high Ca^{2+}-affinity of CBP40Δ, as demonstrated by a deletion mutant [1].

The concentration of Ca^{2+} ([Ca^{2+}]) in the protoplasm is about 10^{-7} M, and [Ca^{2+}] in the extracellular fluid is about 10^{-3} M. Once the plasmodium is wounded, [Ca^{2+}] of the damaged area rises and CBP40 binds Ca^{2+}. Next, CBP40 aggregates and walls off the damaged area. Then, how is the self-assembly of CBP40 regulated by Ca^{2+}? We propose a hypothesis for the regulation mechanism. Helix 1 in the coiled-coil of CBP40Δ is 17 residues shorter than helix 2. According to secondary structure prediction, helix 1 is expected to become the same length as helix 2 in CBP40. Helical wheel analysis reveals that the additional region of helix 1 will make hydrophobic and electrostatic interactions with helix 2.
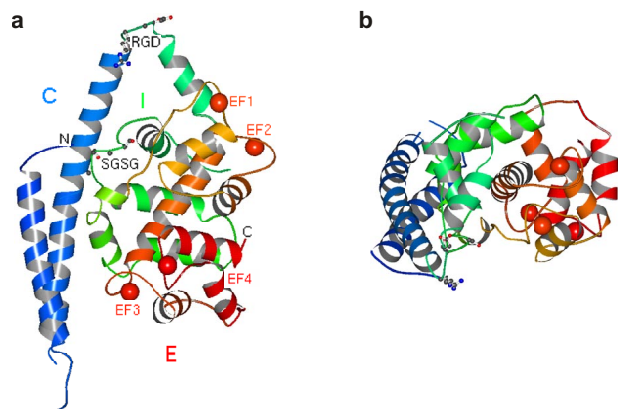
Figure 6
Overall fold of the Ca²⁺-bound form of CBP40Δ. Side (a) and top (b) views are shown. The bound Ca²⁺ ions are represented as spheres. The coiled-coil (C) and intervening (I) domains are shown in blue and green, respectively. EF-hand motifs in the EF-hand (E) domain from EF1 to EF4 are represented by a gradation from orange to red.

The interacting surface between the helices therefore will become much larger than that of CBP40Δ, resulting in a longer intertwined coiled-coil. We propose the mechanism of oligomerization from this structural feature; the extended coiled-coils of CBP40 make intermolecular helical bundles. In CBP40, the small structural change of the EF-hand domain upon Ca²⁺-binding is transmitted to the coiled-coil, and induces the rearrangement of the coiled-coil helices, which enables coiled-coil to make intermolecular helical bundles. The model is shown in Fig. 7. Slight rearrangement of the relative position between coiled-coil helices is enough for making intermolecular four-helix bundles. There are some Gln and Lys residues on the hypothetical intermolecular surface. Recently,
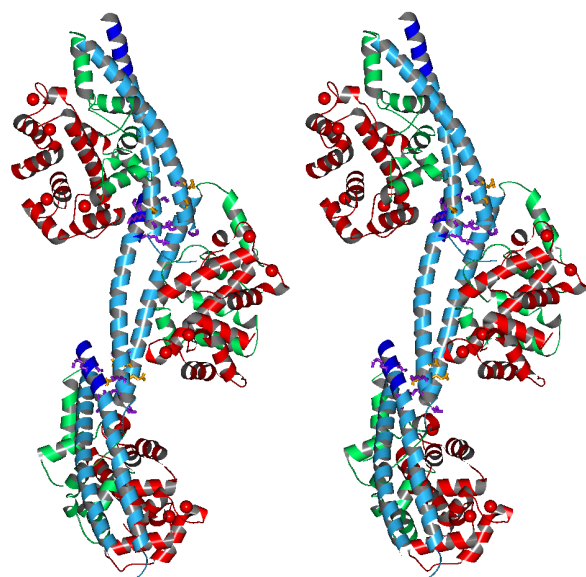
Figure 7
The model of the Ca²⁺-induced oligomer of CBP40 making intermolecular four-helix bundles, shown in stereo view. The coiled-coil, intervening and EF-hand domains are shown in sky blue, green, and red, respectively. The additional N-terminal helix (Ala22-Lys32) is shown in navy blue. Met1-Ala21 are not shown. Gln and Lys residues located on the intermolecular surfaces are shown as stick models in purple and yellow, respectively.

a transglutaminase was purified from plasmodia, and CBP40 was identified as a substrate. These Gln and Lys residues might be cross-linked by transglutaminase to form rigid clumps.

W. Iwasaki[1, 2] and M. Tanokura[1] ([1]Univ. of Tokyo, [2]RIKEN/SPring-8)

References
[1] A. Nakamura, T. Okagaki, T. Takagi, K. Nakashima, M. Yazawa and K. Kohama, *Biochemistry* **39** (2000) 3827.
[2] W. Iwasaki, H. Sasaki, A. Nakamura, K. Kohama and M. Tanokura, *Structure* **11** (2003) 75.
[3] W. Iwasaki, H. Sasaki, A. Nakamura, K. Kohama and M. Tanokura, *J. Biochem.* **126** (1999) 7.

8-5 A Novel Intramolecular Covalent Bond Found in Catalase-Peroxidase

Many microorganisms have catalase-peroxidases which exhibit both catalase and peroxidase activities to defend against oxygen toxicity by removing H_2O_2 from the cell.
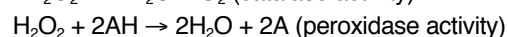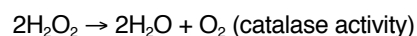
$$2H_2O_2 \rightarrow 2H_2O + O_2 \text{ (catalase activity)}$$
$$H_2O_2 + 2AH \rightarrow 2H_2O + 2A \text{ (peroxidase activity)}$$
$$\text{(AH: substrate such as NADH)}$$

Catalase-peroxidases share an amino acid sequence similarity with monofunctional peroxidases, but not with typical monofunctional catalases such as bovine liver catalase and *Escherichia coli* hydroperoxidases II. Therefore, the catalase-peroxidase is classified as a member of the class I peroxidase superfamily, and its heme environment at the active site has been speculated to be similar to that of typical monofunctional peroxidases such as yeast cytochrome *c* peroxidase (CCP) and eukaryotic ascorbate peroxidase (APX) [1]. The present research has been undertaken to throw light on the structure of catalase-peroxidase which acquires catalase activity in addition to peroxidase activity.

The crystal structure of the catalase-peroxidase from halophilic archaea, *Haloarcula marismortui*, (*Hm*CP) has been determined at 2.0 Å resolution [2]. An asymmetric unit of the *Hm*CP crystal contains two identical subunits, each of which binds one heme b and ~700 solvent molecules (Fig. 8). Consistent with predictions from sequence analysis, each subunit is organized into two structurally similar domains. The topological arrangement of secondary structural elements in the two domains is identical to those of CCP and APX. There are three additional large loops in the N-terminal domain of *Hm*CP. Due to these loops, the heme is buried inside the enzyme, and substrate access to the active site is through a narrow channel that prevents the access of a large substrate. The arrangement of a buried heme active site is similar to that in monofunctional catalases but is different from that in peroxidases.
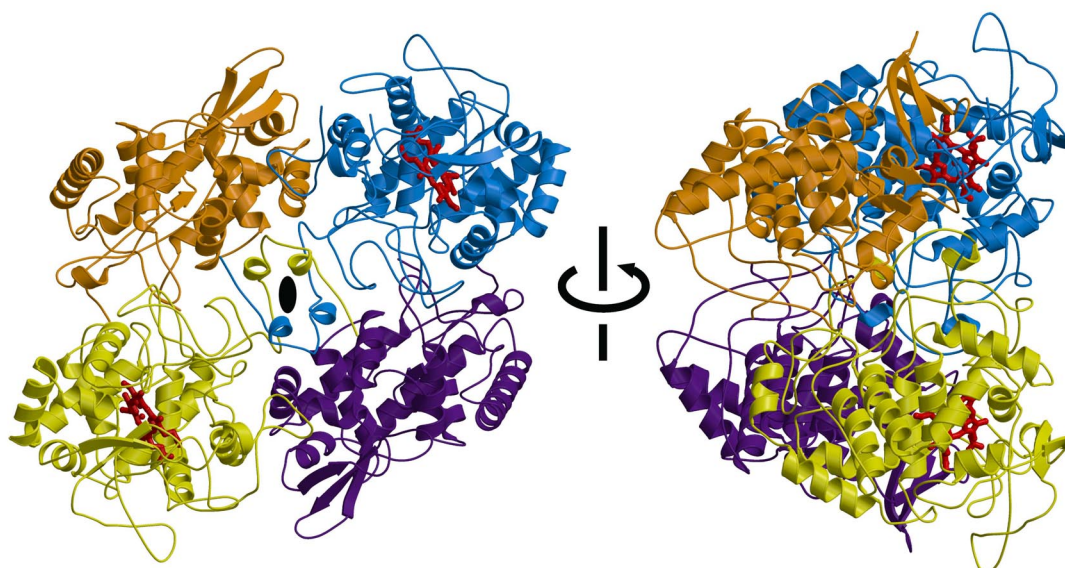
Figure 8
Two views of the dimer related by a 90° rotation. The N- and C-terminal domains of each subunit 1 are purple and blue, respectively, whereas those in subunit 2 are yellow and gold, respectively. The noncrystallographic two-fold symmetry in the dimer is represented by a black ellipse. Heme *b* is shown as a red stick model.
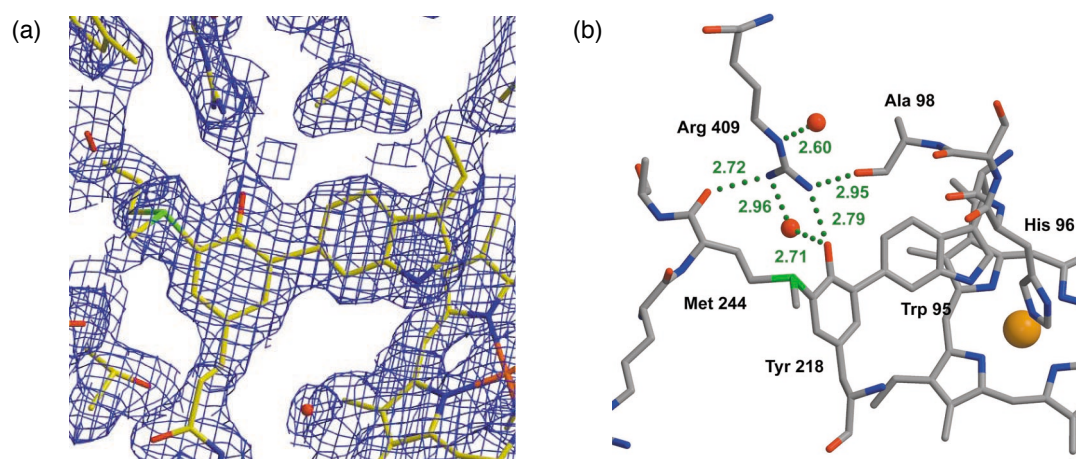

Figure 9
Active site structure. (a) The 2Fo-Fc omit maps for the region of Trp95, Tyr218 and Met244 contoured at 2.0σ level. (b) The environment of Arg409. Red and orange spheres represent water molecules and the iron atom of the heme, respectively. Hydrogen bonds are represented as green dotted lines. Distances (Å) between the hydrogen bonding atoms are labeled.

In the vicinity of the active site of *Hm*CP, continuous electron density is observed between $O\varepsilon 1$ of Tyr218 and $C\eta 2$ of Trp95, and between $O\varepsilon 2$ of Tyr218 and $S\delta$ of Met244 in each subunit of the dimer (Fig. 9(a)). Regardless of whether the model was refined with or without steric restraint among the three side chains, the electron density map indicates the existence of covalent bonds between these side chains. These novel covalent bonds have not been reported previously. The guanidino group of Arg409 forms hydrogen bonds with $O\eta$ of Tyr218 and with the amide nitrogen atom of Met244. These hydrogen bonds stabilize the covalent bond between Tyr218 and Met244 by fixing the relative positions of these residues (Fig. 9(b)). Tyr218 anchors one of the large loops on the molecular surface by forming covalent bonds. The con-

servation of Trp95, Tyr218, Met244 and Arg409 suggests that the novel covalent bonds observed in *Hm*CP may be common in other catalase-peroxidases. Furthermore, these covalent bonds may be important for the catalase activity of the catalase-peroxidase because only the catalase activity is lost upon mutation of Trp95 [3].

**Y. Yamada[1] and N. Tanaka[2] ([1]KEK-PF, [2]Tokyo Inst. of Tech.)**

References
[1] K.G. Welinder, *Biochim. Biophys. Acta* **1080** (1992) 215.
[2] Y. Yamada, T. Fujiwara, T. Sato, N. Igarashi and N. Tanaka, *Nature Struct. Biol.* **9** (2002) 691.
[3] M. Zamocky, G. Regelsberer, C. Jakopitsch and C. Obinger, *FEBS Lett.* **492** (2001) 177.

8-6 Crystal Structure of the First Natural Diels-Alderase, Macrophomate Synthase

The Diels-Alder reaction is a cycloaddition whose mechanism involves the overlap of the π-orbitals of the two unsaturated systems in which an alkene (dienophile) adds to a 1,3-diene to form a 6-membered ring. The reaction is synthetically very useful because it forms cyclic products with high regio- and stereoselectivity under mild conditions [1]. It has been applied to the synthesis of complex pharmaceutical and biologically active compounds. Catalytic methods with biomolecules such as RNA and protein antibody have also been developed. The reactions catalyzed by these biomolecules show remarkable enantio- and diastereoselectivity. Recently, natural Diels-Alderases such as solanapyrone synthase [2], lovastatin nonaketide synthase [3] and macrophomate synthase [4] (MPS) have been reported in the biosynthesis of secondary natural products. The function and catalytic mechanism of the natural Diels-Alderase are of great interest due to the diversity of molecular skeletons in natural Diels-Alder adducts [5]. However, the details of the catalysis of natural Diels-Alderases are still poorly understood.

The phytopathogenic fungus, *Macrophoma commelinae*, isolated from spots on the leaves of *Commelina communis* has the ability to transform 2-pyrone derivatives into the corresponding benzoate analogues [6] (Fig. 10). This complex aromatic conversion is catalyzed by only one enzyme, macrophomate synthase (MPS), with oxalacetate as a substrate for the C3-unit precursor. MPS is a Mg^{2+}-dependent enzyme with 339 amino acid residues (Mw = 36244 Da) [7], the sequence of which showed no significant similarity with known proteins in a homology search. The catalytic mechanism of
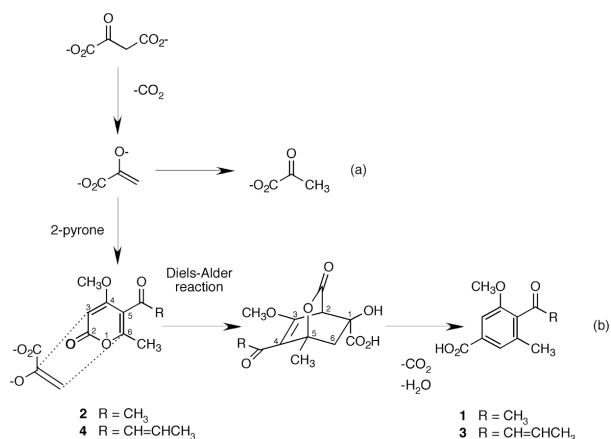
Figure 10
Enzymatic reactions catalyzed by MPS. (a) Decarboxylation without 2-pyrone. (b) Multi-step transformation with 2-pyrone. Macrophomate **1** and 2-pyrone **2** have been discovered in *Macrophoma commelinae*. MPS also can covert Pyrenocin A **4** into pyrenocheatic acid A **3**, which are phytotoxins from onion pink rot.
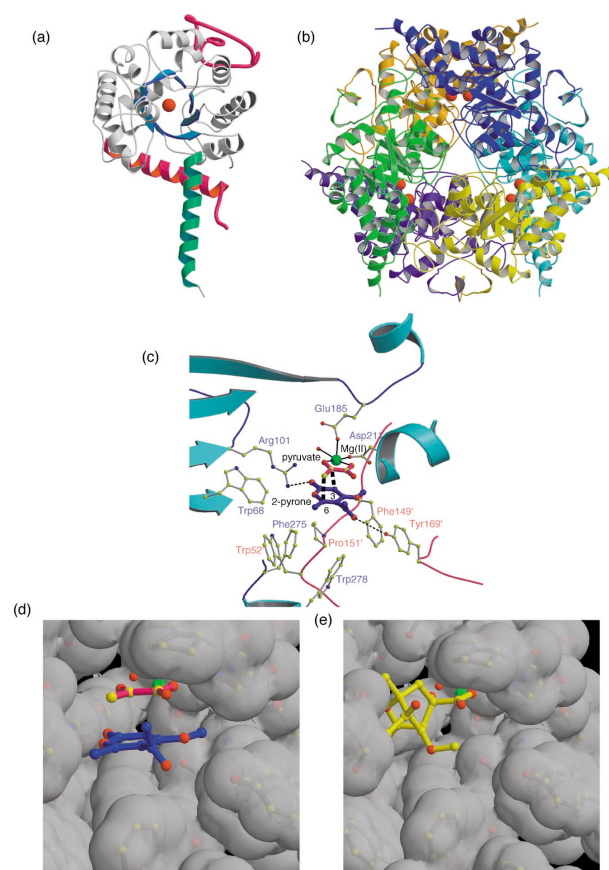
Figure 11
(a) Protomer structure of MPS showing the α-helix swapped $(β/α)_8$ barrel fold. The core β-barrel (blue) is surrounded by 11 α-helices. The long α8-helix (colored in magenta) belongs to the neighboring protomer related by the 2-fold axis and joins to the β-barrel core to form a complete $(β/α)_8$ barrel. (b) The functional unit of MPS with point group symmetry 32. (c) The residues in the active site pocket and proposed model for the very early transition state of the Diels-Alder reaction. 2-pyrone **2** (blue thick bond) is placed in parallel with pyruvate enolate (red thick bond) which is bound to Mg^{2+} (green ball). (d) The space-filling model of the active site with transition state of substrates pyruvate enolate (red) and 2-pyrone **2** (blue) and (e) reaction intermediate bicyclo[2,2,2]octane (yellow). The active site is delicately engraved for the entropy trap Diels-Alder reaction.

the whole pathway was investigated extensively, and it was shown that it proceeds through three separate steps including decarboxylation, two carbon-carbon bond formations, and decarboxylation with concomitant dehydration. In the absence of 2-pyrone, MPS simply acts as a decarboxylase with high catalytic efficiency (Fig. 10(a)). Furthermore, the involvement of a Diels-Alder reaction at the second step is proposed [4], based on the previously reported reaction type and the stereospecificity of the reaction. We present the first atomic resolution structure of a natural Diels-Alderase.

The molecule is hexameric with point group symmetry 32. The protomer core region consists of an 8 stranded β-barrel surrounded by 8+3 α-helices with a $(β/α)_8$ barrel fold. The C-terminal α8-helix (residues 275-298) of each protomer protrudes from the core and joins to the β-barrel of the 2-fold-related protomer (Fig. 11(a)). With these swapped helices two protomers are closely associated to form an extensively hydrophobic dimer interface (Fig.

11(b)).

In the second step of the reaction, the cycloaddition of the enolate and the 2-pyrone takes place (Fig. 10). The steric congestion of the peptide backbone allows the 2-pyrone access only from one side of the enolate plane where the catalytic pocket is open. Figure 11(c,d) shows the proposed model for the very early transition state of the Diels-Alder reaction. In this binding model, two planes (2-pyrone and pyruvate enolate) are placed in parallel at π-orbital-overlapping distance. Several features are worth noting in this model. First, the 2-pyrone molecule is likely to be fixed in place through two hydrogen bonds between the carbonyl oxygen of 2-pyrone and Arg101, and the C5-acyl oxygen and Tyr169. Tyr169 is in turn placed in the proper orientation via stacking with Phe149. The flexible loop (residues 139-170) with hydrophobic side-chains (Phe149, Pro151 and Trp152) from the 3-fold-related protomer shields this transition state from the solvent. The stacking direction of 2-pyrone to pyruvate enolate is exactly the one expected from the product.

Both of R101S and Y169F mutants dramatically disturbed MPS activity while retaining the decarboxylase activity, suggesting the importance of these hydrogen bonds in the carbon-carbon bond-forming reaction. The experimental result that 2-pyrones lacking a C5-acyl group are not converted into normal aromatic products [8] gives further support for this binding structure. Generally speaking, the hydrogen-bonds between LUMO-energied substrate and some moieties in the reaction medium accelerate the Diels-Alder reaction. As shown in Fig. 11(d,e), the intermediate is substantially reoriented from the early transition state with respect to the enzyme because of the conformational constraints imposed upon the adduct. The rather large hydrophobic cavity of this enzyme enables this rotation (reorientation) to occur without any steric congestion. The enzyme also has substantial van der Waals contacts to this intermediate. The first natural Diels-Alderase is found to adopt several such ingenious strategies.

T. Ose, K. Watanabe, M. Yao, H. Oikawa and I. Tanaka (Hokkaido Univ.)

References

[1] W. Carruthers, *Cycloaddition Reactions in Organic Synthesis* (Pergamon, Oxford, 1990).

[2] H.Oikawa, T. Kobayashi, K. Katayama, Y. Suzuki and A. Ichihara, *J. Org. Chem.* **63** (1998) 8748.

[3] J. Kennedy, K. Auclair, S.G. Kendrew, C. Park, J.C. Vederas and C.R. Hutchinson, *Science* **284** (1999) 1368.

[4] K. Watanabe, T. Mie, A. Ichihara, H. Oikawa and M. Honma, *J. Biol. Chem.* **275** (2000) 38393.

[5] A. Ichihara and H. Oikawa, *in Comprehensive Natural Products Chemistry* (eds. D. Barton, K. Nakanishi and O. Meth-Cohn, Elsevier, Amsterdam) **1** (1999) 367.

[6] I. Sakurai, H. Miyajima, K. Akiyama, S. Shimizu and Y. Yamamoto, *Chem. Pharm. Bull.* **36** (1998) 2003.

[7] K. Watanabe, H. Oikawa, K. Yagi, S. Ohashi, T. Mie, A. Ichihara and M. Honma, *J. Biochem.* **127** (2000) 467.

[8] K. Watanabe, T. Mie, A. Ichihara, H. Oikawa and M. Honma, *Biosci. Biotechnol. Biochem.* **64** (2000) 530.

8-7 Crystal Structures of the Reaction Intermediate and its Homologue of an Extradiol-Cleaving Catecholic Dioxygenase

Extradiol-cleaving catecholic dioxygenases (hereafter extradiol dioxygenases) are enzymes that play a key role in the degradation pathway of aromatic compounds. These enzymes catalyze the addition of two atomic oxygens to the catechol ring of the substrate, resulting in cleavage of the catechol ring. Extradiol dioxygenases typically contain a non-heme iron (Fe^{II}) in their active site, which is easily oxidized into Fe^{III} under aerobic conditions. The oxidation of the Fe ion inactivates the enzymatic reaction. BphC is an extradiol dioxygenase derived from *Pseudomonas* sp. strain KKS102. Previously, we have determined the crystal structures of BphC and its substrate complex using inactive form enzymes [1,2]. These crystal structures revealed details of the extradiol dioxygenase's active site, but high-resolution crystal structures with the active form enzyme are essential to precisely discuss the reaction mechanism of the enzyme. Here we report high-resolution crystal structures of BphC in substrate-free form, the BphC-substrate complex (the ES complex) and the BphC-substrate-NO complex (the ES-NO complex) [3,4].

The BphC used in the present study was reactivated just before crystallization [3]. The reactivated BphC was then crystallized under anaerobic conditions. The crystals of ES and ES-NO complexes were prepared using the soaking method under anaerobic conditions. Diffraction data of these crystals was collected at 100 K using the ADSC 2×2 CCD detector installed either at BL-6A or BL-18B. Crystal structures of BphC (substrate free form) and the ES-complex were determined at 1.45 Å resolution with R-factors of 16.1% and 16.3%, respectively. The crystal structure of the ES-NO complex was determined at 2.0 Å resolution (R-factor = 16.1%) [4] (Fig. 12).

The crystal structures revealed the followings. (A) The substrate (2,3-DHBP) directly coordinates to the Fe ion as a monoanionic form (Fig.12(b)). (B) Upon substrate binding, His194, which is indispensable for the catalytic reaction [5], makes a conformational change, forming a strong hydrogen bond with the hydroxyl group of the substrate (Fig.12(b)). (C) The NO molecule directly coordinates to the Fe ion (Fig.12(c)). The binding site of the NO molecule, which is highly likely to be the binding site of a dioxygen, is the vacant site of the octahedral coordination sphere of the ES complex.

On the basis of the present crystal structures, we propose a catalytic mechanism for BphC [4] (Fig. 13). In this mechanism, His194 seems to play three distinct roles. At the early stage of the catalytic reaction, His194 appears to act as a catalytic base, which likely deprotonates the
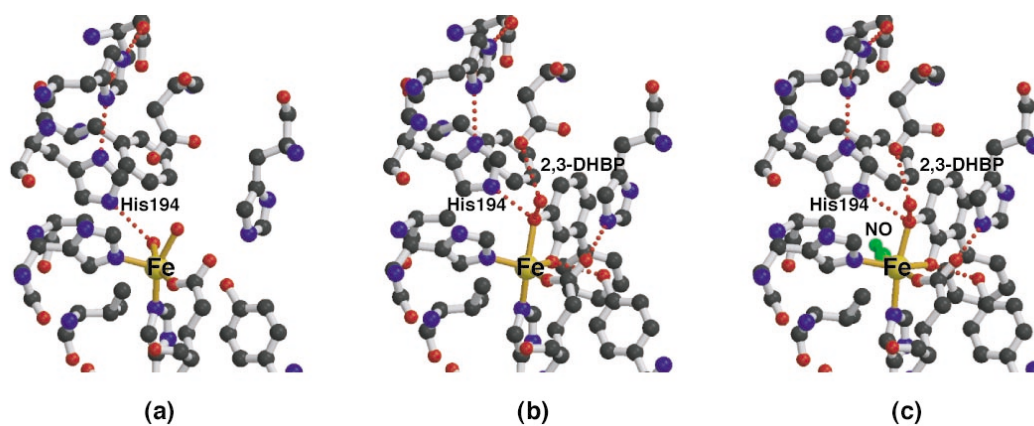
Figure 12
Active-site structure of (a) the substrate-free form, (b) the ES complex, and (c) the ES-NO complex. Hydrogen bonds are shown as red dotted lines. The NO molecule is shown in green.
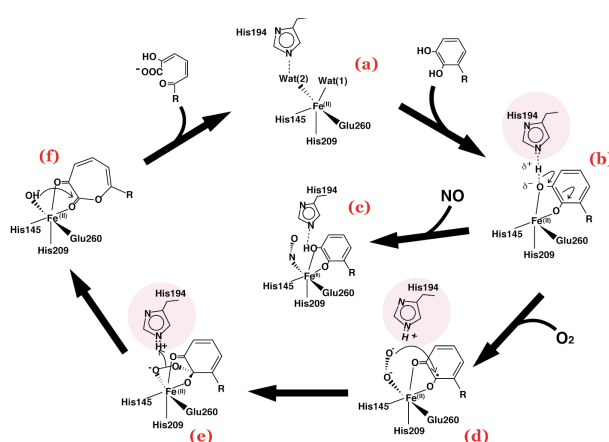

Figure 13
Proposed mechanism for extradiol ring cleavage of 2,3-DHBP by BphC. The ES-NO complex is presented in the center.

hydroxyl group of the substrate (Fig. 13(b)). At the next stage, the protonated His194 seems to stabilize a negative charge on the O_2 molecule located in the hydrophobic O_2-binding cavity (Fig. 13(d)). Finally, the protonated His194 seems to function as a proton donor (Fig. 13(e)).

T. Senda (AIST)

References
[1] K. Sugiyama, T. Senda, H. Narita, T. Yamamoto, K. Kimbara, M. Fukuda, K. Yano and Y Mitsui, *Proc. Japan Acad.* **71B** (1995) 33.
[2] T. Senda, K. Sugiyama, H. Narita, T. Yamamoto, K. Kimbara, M. Fukuda, M. Sato, K. Yano and Y. Mitsui, *J. Mol. Biol.* **255** (1996) 735.
[3] Y. Uragami, T. Senda, K. Sugimoto, N. Sato, V. Nagarajan, E. Masai, M. Fukda and Y Mitsui, *J. Inorg. Biochem.* **83** (2001) 269.
[4] N. Sato, Y. Uragami, T. Nishizaki, Y. Takahashi, G. Sazaki, K. Sugimoto, T. Nonaka, E. Masai, M. Fukuda and T Senda, *J. Mol. Biol.* **321** (2002) 621.
[5] T. Senda, K. Sugimoto, T. Nishizaki, M. Okano, T. Yamada, E. Masai, M. Fukuda and Y. Mitsui, *Oxygen Homeostasis and Its Dynamics* (ed. Ishimura) (1997) 276.

8-8 A Directed Evolution Approach to a Structural Genomics Project: Rv2002 from *Mycobacterium tuberculosis*

The expression of target proteins in soluble form remains one of the most serious bottlenecks in structural genomics efforts. As a useful method of overcoming the problem of inclusion body formation in *E. coli* expression, the directed evolution technique was proposed. In this experiment, a library of mutants is generated by error-prone PCR and DNA shuffling, and then soluble mutants are selected using green fluorescent protein (GFP) as a folding reporter. The present work on the *Mycobacterium tuberculosis* Rv2002 gene product demonstrates the utility of the directed evolution approach to structural genomics projects in overcoming the difficulties involved in overexpressing the target proteins in soluble form. The Rv2002 gene encodes a 260-residue protein, which belongs to the short-chain dehydrogenase/reductase (SDR) family. By applying the directed evolution technique, we prepared several soluble mutants of the protein, whereas the wild type was previously expressed as inclusion bodies in *E. coli* [1]. Among the soluble mutants, a triple mutant I6T/V47M/T69K (Rv2002-M3) was chosen for downstream structural and functional characterizations (Fig. 14(a)), since it showed a maximum improvement in solubility and contained the smallest number of point mutations which fall outside the conserved regions in the primary sequence. Enzymatic assays indicate that the Rv2002-M3 protein has a high catalytic activity as an NADH-dependent 3α, 20β-hydroxysteroid dehydrogenase.

We have determined the crystal structures of a binary complex with NAD$^+$ and a ternary complex with androsterone and NADH (Fig. 14(b)). The structure reveals that Asp38 determines the cofactor specificity. The catalytic site includes an unusual Glu142 as well as a canonical catalytic triad of the SDR family, Ser140/Tyr153/Lys157. Enzymatic assays of the E142A mutant of Rv2002-M3
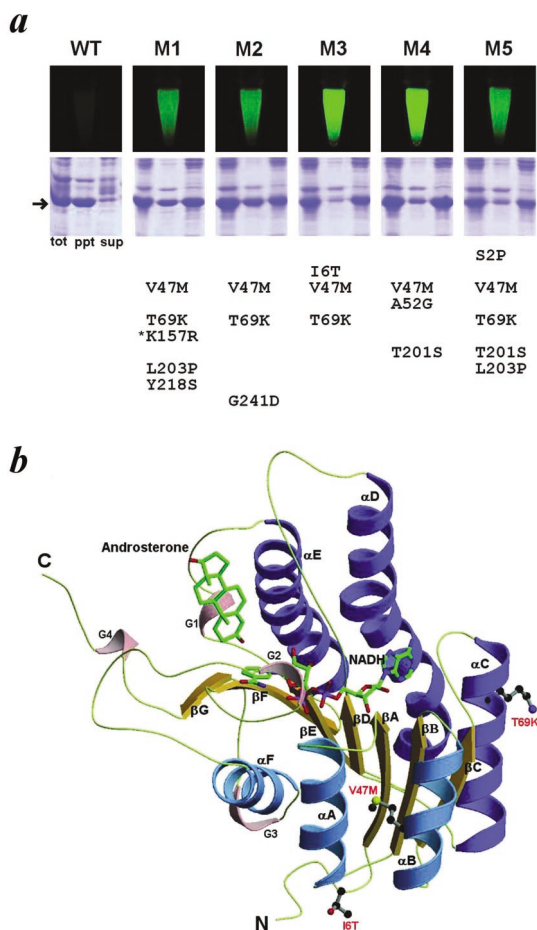
Figure 14
GFP-based directed evolution and overall subunit structure of the Rv2002-M3 protein. (a) Fluorescence of the resuspended cells harboring genes encoding the wild type or mutant Rv2002 proteins in a GFP-fused form and expression test of the wild type or mutant Rv2002 proteins in a non-fused form. WT, wild type; M1-M5, soluble mutants. tot, total cell; ppt, precipitant fraction; sup, supernatant fraction. The arrow indicates the expressed Rv2002 proteins and the asterisk signifies the mutation at a conserved residue of the SDR family. (b) Ribbon diagram of the Rv2002-M3 monomer in complex with NADH and androsterone.

indicate that Glu142 reverses the effect of Lys157 in influencing the pKa of Tyr153. This study raises the possibility that the Rv2002 gene product could be involved in steroid metabolism in *M. tuberculosis* as a unique member of the SDR family. T69K and I6T mutations could possibly increase the intrinsic solubility of the folded protein, since these substitutions occurring on the molecular surface enhance the polar characteristics of the molecule. The mutation V47M contributes to a tighter packing of the subunit hydrophobic core and consequently to the overall stability of the subunit. A major role of V47M mutation may be to lower the kinetic barrier in the folding pathway. All single mutants (I6T, V47M, T69K) were mostly insoluble, whereas two of the double mutants (I6T/V47M, V47M/T69K) were highly soluble.

J.K. Yang[1], M.S. Park[2], G.S. Waldo[2] and S.W. Suh[1]
([1]Seoul Natl. Univ., [2]Los Alamos Natl. Lab.)

References
[1] J.K. Yang *et al.*, *Proc. Natl. Acad. Sci. USA* **100** (2003) 455.

8-9 Equilibrium and Kinetics of the Allosteric Transition of the Chaperonin GroEL Studied by Solution X-Ray Scattering

The GroEL from *Escherichia coli*, a tetradecameric protein complex of 14 identical 57-kDa subunits arranged in two heptameric rings stacked back-to-back with a central cavity, is one of the best characterized molecular chaperones (Fig. 15). The ATP-dependent control of the affinity of GroEL for its target protein and the resulting facilitation of protein folding are underpinned by the allosteric transitions of GroEL induced by ATP. However, these allosteric transitions have so far only been investigated by the ATPase assay of GroEL or by fluorescence spectroscopy of tryptophan mutants of GroEL, and there is no direct structural data for the real-time allosteric transitions in solution. Therefore, a number of mysteries remain unsolved, especially concerning the structural characteristics and the kinetics of the allosteric transitions. Another method, which can monitor directly the global structural changes of the protein molecule in real time, is certainly required if we are better to understand the allosteric mechanisms of GroEL.

Small-angle X-ray scattering (SAXS) is a powerful
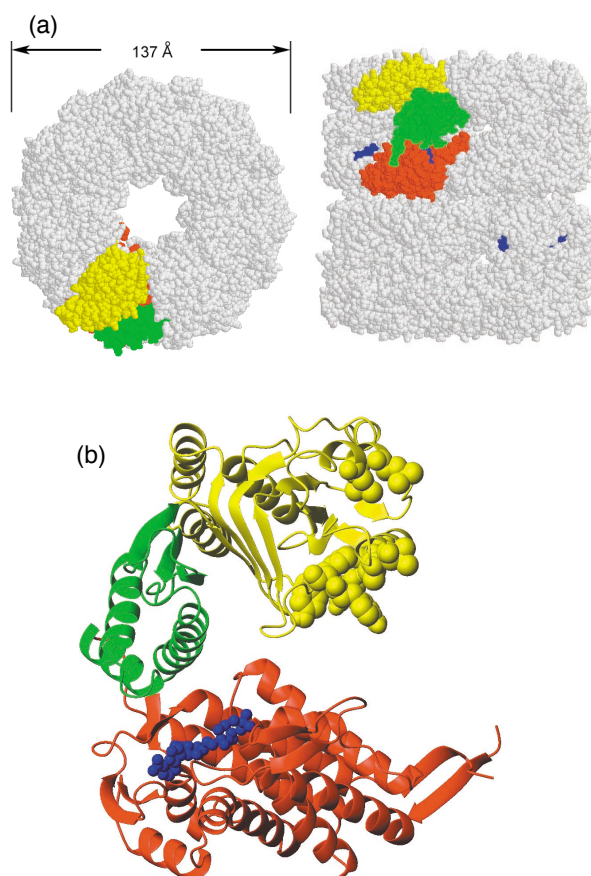
Figure 15
X-ray crystallographic structure of GroEL (PDB: 1KP8). (a) The 14-mer structure: the top view (left) and the side view (right). (b) The structure of a single subunit. The apical (yellow), intermediate (green) and equatorial (red) domain are shown. The nucleotide (ATPγS) is shown in blue.

technique for studying directly any changes in the size and shape of a protein molecule and a protein complex in solution, and this technique should complement the structural information acquired via other spectroscopic (fluorescence, circular dichroism, *etc.*) techniques and via enzymatic assay. Recently, the use of synchrotron radiation has made it possible to combine a stopped-flow technique with SAXS measurements. Furthermore, combination of the SAXS technique with a two-dimensional (2D) charge-coupled device (CCD)-based X-ray detector has made it possible to improve the signal-to-noise (S/N) ratio of the stopped-flow SAXS data dramatically. This new technique should be useful for investigating the allosteric transitions of large protein complexes [1,2].

In the present study, we have investigated the ATP-induced allosteric transitions of GroEL with static and stopped-flow SAXS [3,4]. The results of the SAXS measurements show that the three allosteric states (the TT, the TR, and the RR states) are structurally different from each other (Fig. 16(a)); the two rings of GroEL assume two allosteric states, T (tense) and R (relaxed), depend-ing on ATP concentration, and hence there are three alloateric states, TT, TR and RR, for the GroEL particle. The kinetics of the TT to TR transition has been observed for the first time directly using stopped-flow SAXS. The rate constant of the transition is 3.4 s^{-1} (85 μM ATP and 4.8ºC) (Fig. 16(b)), and hence this is shown to correspond to the second phase of the ATP-induced kinetics of tryptophan-inserted GroEL previously measured by stopped-flow fluorescence. We have also found by fluorescence spectroscopy that the first phase is a bimolecular process caused by non-cooperative binding of ATP to GroEL with a bimolecular rate constant of 5.8×10^5 M^{-1}s^{-1}. The ATP-induced cooperative transition observed by fluorescence as well as SAXS measurements at low concentration of ATP (< 400 μM) is well explained by a kinetic Monod-Wyman-Changeux (MWC) model that is a combination of the conventional transition state theory and the basic MWC model.

K. Kuwajima (Univ. of Tokyo)

References
[1] K. Ito and Y. Amemiya, *J. Jpn. Soc. Synchrotron Rad. Res.* **13** (2000) 372 (in Japanese).
[2] M. Arai, K. Ito, T. Inobe, M. Nakao, K. Maki, K. Kamagata, H. Kihara, Y. Amemiya and K. Kuwajima, *J. Mol. Biol.* **321** (2002) 121.
[3] T. Inobe, M. Arai, M. Nakao, K. Ito, K. Kamagata, T. Makio, Y. Amemiya, H. Kihara and K. Kuwajima, *J. Mol. Biol.* **327** (2003) 183.
[4] T. Inobe, K. Kikushima, T. Makio, M. Arai and K. Kuwajima, *J. Mol. Biol.* **329** (2003) 121.

8-10 Light-Induced Conformational Change of Photoactive Yellow Protein

Photoactive yellow protein (PYP), a photoreceptor protein found in the purple phototrophic bacterium, *Ectothiorhodospira halophila*, acts as a blue-light receptor for the negative phototaxis of the bacterium. The chromophore of PYP, a thioester-linked trans-*p*-coumaric acid, is isomerized to the *cis*-form upon photon absorption and PYP undergoes a photocycle. Among the photocycle intermediates, the last one (PYP$_M$), whose absorption band is located in the near-UV region, is considered to be in a physiologically active form. The structure of PYP$_M$ has been analyzed by time-resolved crystallography [1]. The structural difference between PYP and PYP$_M$ in the crystal form is limited to the region around the chromophore. However, accumulated evidence strongly suggests that the structural change under physiological conditions is much larger than that in the crystal, probably because conformational change is restricted in the crystal. We have examined the light-induced conformational change of PYP in solution by small-angle X-ray scattering (SAXS) [2].
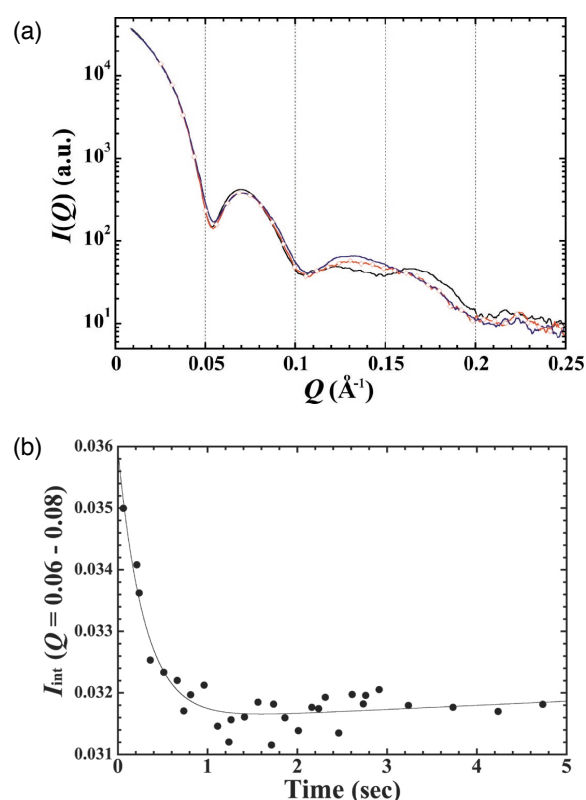
PYP was heterologously overexpressed by

Figure 16
(a) SAXS patterns of GroEL at 0 M (TT) (black line), 85 μM (TR) (red line with open circles), and 3 mM ATP (RR) (blue line) at 25°C. The scattering intensity $I(Q)$ is shown as a function of Q. (b) Kinetic curve of the ATP-induced structural change of GroEL at 4.8°C monitored by integral intensity, I_{int}. The integral region of Q employed was from 0.06 Å^{-1} to 0.08 Å^{-1}. The structural change was initiated by mixing with ATP (final concentrations of 3.8 μM (3 mg/ml) and 85 μM for GroEL and ATP, respectively). The solid line is a theoretical kinetic progress curve assuming a single exponential with the equation: $I_{int}(t) = Ae^{-kt} + Bt + C$, where A and k are the amplitude and the rate constant of the exponential phase and B and C are constants. The second term Bt is introduced for the purpose of correcting for the linear increase in the scattering intensity caused by beam damage.

Escherichia coli, and reconstituted by adding *p*-coumaric anhydride. Because of the short lifetime of PYP_M (~100 ms), its characterization is difficult. To stabilize PYP_M, the N-terminal 6, 15 or 23 amino acid residues of PYP were truncated by bovine pancreas chymotrypsin (T6, T15 and T23, respectively). Systematic characterization of the truncated PYPs provided information on the structural change in the N-terminal region. The SAXS measurements were carried out at BL-10C.

The square of the radius of gyration (R_g^2) of PYPs in the dark was estimated by a Guinier plot (Fig. 17). Values of R_g^2 for T6, T15, and T23 under illumination ($T6_M$, $T15_M$, and $T23_M$) were similarly estimated. The R_g^2 values for the dark states were slightly decreased by truncation. Upon illumination, the R_g values of truncated PYPs were markedly increased. The increase in R_g by illumination was 1.1 Å for T6 and 0.7 Å for T15 and T23. It should be noted that the difference in R_g between T6 and T15 was 0.3 Å, but that between $T6_M$ and $T15_M$ it was 0.7 Å. In contrast, the difference in R_g between T15 and T23 was 0.6 Å for both dark and light conditions. Namely, the decrease of R_g by removal of Gly7-Leu15 in the M state was larger than that in the dark state, but that of Ala16-Leu23 was constant. Therefore, Gly7-Leu15 in $T6_M$ is more responsible for R_g than it is in T6. This means that Gly7-Leu15 in the dark state is located more proximately

Figure 18
Structure of PYP in the dark (PDB: 2PHY). Chromophore is colored in yellow. Chymotrypsin-cleavage sites are shown by scissors. The present experiment suggested that N-terminal loop is detached from the β-sheet upon formation of PYP_M.

to the center than in the M intermediate. In the dark state, Gly7-Leu15 forms a short α-helix which lies parallel to the plane of the β-sheet (Fig. 18). The present data can be explained by a model in which the N-terminal loop is detached from the β-sheet upon the formation of PYP_M. The structural change for formation of PYP_M is not merely a rearrangement of the surface charge distribution but involves a global conformational change, resulting in increases in the dimensions and changes in the shape. This may enable the interaction with other molecules such as membrane and proteins.

Y. Imamoto and M. Kataoka (Nara Inst. of Sci. Tech.)

References
[1] U.K. Genick, G.E. Borgstahl, K. Ng, Z. Ren, C. Pradervand, P.M. Burke, V. Srajer, T.Y. Teng, W. Schildkamp, D.E. McRee, K. Moffat and E.D. Getzoff, *Science* **275** (1997) 1471.
[2] Y. Imamoto, H. Kamikubo, M. Harigai, N. Shimizu and M. Kataoka, *Biochemistry* **41** (2002) 13595.

8-11 Energy Transducing Conformation Changes of Myosin Motor Proteins

Elucidating the mechanism by which the actin-myosin motor system transduces the chemical energy of ATP hydrolysis to power the movement of animals and cells remains one of the major challenges in biological science. Skeletal muscle myosin (myosin II) consists of two globular heads linked by helical segments that supercoil to form a long helical rod. The rod segments assemble into the shaft of the myosin filaments, and the head portions project outward towards the actin filaments, forming the crossbridges that are responsible for the generation of a sliding force between the two filaments. Myosin heads play a key role in converting chemical energy in the form of ATP into mechanical energy driving the directional motion of myosin heads relative to the actin filaments. It has
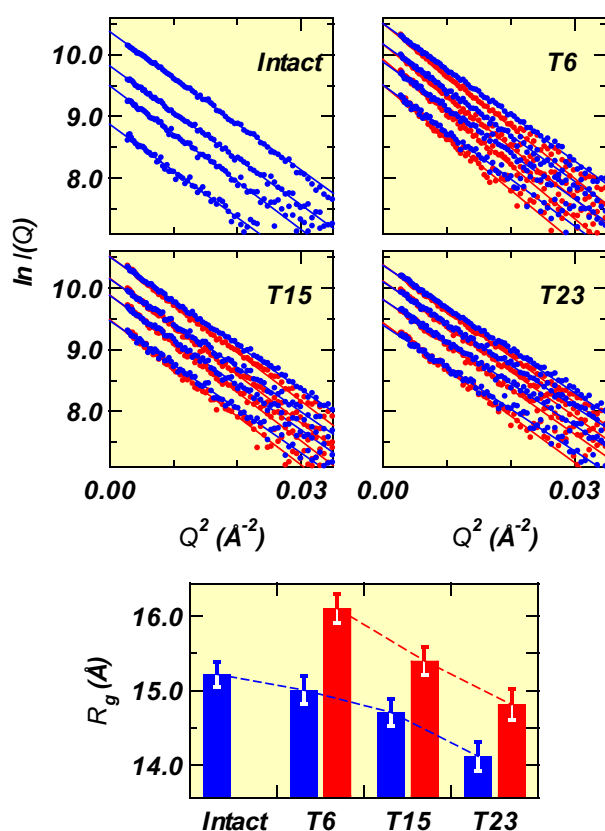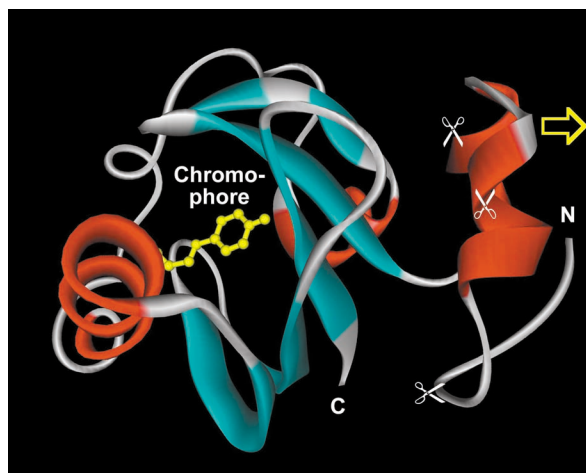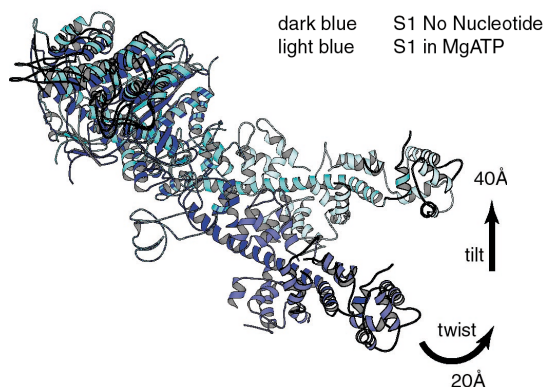

Figure 17
Guinier plots of intact PYP, T6, T15, and T23 in the dark (blue) and under continuous illumination with >410 nm light (red). The protein concentrations were 10, 6, 4, and 2 mg/ml (from top to bottom) for intact PYP, 12, 8, 6, and 4 mg/ml for T6 and T15, and 10, 8, 6, and 4 mg/ml for T23. Bottom panel: Comparison of R_g in the dark (blue) and with light (red).

| dark blue | S1 No Nucleotide |
| light blue | S1 in MgATP |

40Å

tilt

twist

20Å

Figure 19
The global conformational change of the myosin head (S1) during energy transduction. The motion of the light chain binding domain of S1 involves a tilt and a slew. The S1 molecule is shown with its catalytic domain facing the actin filament axis.

long been expected for the crossbridge mechanism of the acto-myosin motor system that global conformational changes of myosin heads interacting with actin occur in coupling with an ATP hydrolysis reaction. Prior to X-ray crystallographic studies, X-ray solution scattering of isolated myosin heads (subfragment 1, S1) first indicated that the long α-helical regulatory domain containing two light chains deformed globally relative to its catalytic domain during the ATPase cycle [1]. The deformation involves both a tilt and a twist, resulting vectorially in a 5-nm spinning of the distal end of the regulatory domain (Fig. 19) [2,3].

Recently, X-ray scattering studies of S1s with various nucleotide analogs mimicking the reaction steps along the ATPase cycle of S1 have been performed at the Photon Factory small-angle X-ray scattering beamline. The data showed that S1 has distinctly different conformations in the presence of various analogs, implying that the myosin heads alter their conformation depending upon the bound nucleotides (Fig. 20) [4-7]. As summarized in Fig. 20, a large conformational change of the regulatory domain of S1 occurs in a lever arm-like fashion both in the S1*.ATP and S1+.ADP states before and after the key intermediate state (S1**.ADP.Pi) of its ATPase cycle. The direction of

motion of the regulatory domain is opposite to that occurring in the S1**.ADP.Pi state. When an actin filament is present, the contractile or sliding force is thought to be produced in the transition from an S1**.ADP.Pi state to an S1+.ADP state, that is, in the phosphate release step. The present results may indicate a working stroke of myosin heads amounting to ca. 10 nm in this transition. Recent X-ray crystallographic analysis of S1s from invertebrate muscle myosin with various nucleotide analogs has suggested the possible atomic mechanism of such a global movement of the regulatory domain. Support for such a lever arm hypothesis for the motor action of myosin heads is found in recent time-resolved X-ray diffraction and quick-freezing electron microscopic studies from contracting muscle fibers. On the other hand, we have stressed that the elastic dynamics of thin actin filaments is important for the acto-myosin motor activity under the action of myosin heads [8]. Coordinated conformational changes of actin and myosin are clearly required to perform efficient energy transduction in the acto-myosin motor system.

Y. Sugimoto, T. Arata and K. Wakabayashi (Osaka Univ.)

References
[1] K. Wakabayashi, M. Tokunaga, I. Kohno, T. Hamanaka, Y. Takezawa, T. Wakabayashi and Y. Amemiya, *Science* **258** (1992) 443.
[2] Y. Sugimoto, M. Tokunaga, Y. Takezawa, M. Ikebe and K. Wakabayashi, *Biophys. J.* **68** (1995) 29S.
[3] Y. Sugimoto and K. Wakabayashi, *Protein, Nucleic Acid, Enzyme*, **44** (1999) 1605.
[4] Y. Sugimoto, M. Tokunaga and K. Wakabayashi, *Photon Factory Activity Report* **1996 #14** (1997) 334.
[5] Y. Sugimoto, T. Okumura, T. Arata, Y. Takezawa and K. Wakabayashi, *Photon Factory Activity Report* **2000 #18** (2001) B233.
[6] T. Okumura, T. Arata, Y. Sugimoto, Y. Takezawa, M. Kiyotoshi and K. Wakabayashi, *Photon Factory Activity Report* **2001 #19** (2003) B203.
[7] Y. Sugimoto *et al.*, to be published.
[8] Y. Takezawa, Y. Sugimoto and K. Wakabayashi, *Photon Factory Activity Report* **2000 #18** (2001) A41.

state	S1 ⇌ S1. ATP ⇌ S1*. ATP ⇌ S1**. ADP. Pi ⇌ S1†. ADP ⇌ S1. ADP
sample	S1 no nucleotide	S1+MgAMPPNP S1+MgPPi	S1.ADP-*p*PDM	S1+MgATP (~20°C)	S1+MnATP (~4°C)	S1+MnADP (~4°C) S1+MgADP (~20°C)
Rg (Å)	47.8±0.2	48.4±0.1	50.7±0.4	45.7±0.8	51.4±0.6	48.1±0.2
Dmax (Å)	~160	~160	~170	~150	~170	~155
model	0 nm	5 nm	10 nm	10 nm	5 nm

Figure 20
Global motion of the light chain binding domain of S1 with various nucleotide analogs mimicking the intermediate steps of the myosin ATPase reaction. The radius of gyration value (Rg) and the maximum chord length (Dmax) of S1 with and without nucleotides were obtained respectively from Guinier plots and the p(r) functions of the X-ray solution scattering data. The top row of the table shows the representative intermediate states along the ATPase reaction of S1. The movement direction and magnitude of the distal end of the light chain binding domain are shown with an arrow and a value relative to the S1 with no nucleotide or the S1.ATP state in each transition of the states in the bottom row of the table. In the second row, AMPNP is adenyllimidodiphosphate, PPi is pyrophosphate and S1.ADP-*p*PDM is an S1 trapping ADP by *p*PDM (*p*-phenylenedimaleimide) which croslinks two reactive Cysteine residues (SH1 and SH2) of S1.